Soft Matter

RSC Publishing

COMMUNICATION

View Article Online
View Journal | View Issue

Harnessing instabilities for design of soft reconfigurable auxetic/chiral materials†

Cite this: *Soft Matter*, 2013, **9**, 8198

Received 25th April 2013
Accepted 30th May 2013

DOI: 10.1039/c3sm51148k

www.rsc.org/softmatter

Jongmin Shim,‡[b] Sicong Shan,‡[a] Andrej Košmrlj,[c] Sung H. Kang,[a] Elizabeth R. Chen,[a] James C. Weaver[d] and Katia Bertoldi*[ae]

Most materials have a unique form optimized for a specific property and function. However, the ability to reconfigure material structures depending on stimuli opens exciting opportunities. Although mechanical instabilities have been traditionally viewed as a failure mode, here we exploit them to design a class of 2D soft materials whose architecture can be dramatically changed in response to an external stimulus. By considering geometric constraints on the tessellations of the 2D Euclidean plane, we have identified four possible periodic distributions of uniform circular holes where mechanical instability can be exploited to reversibly switch between expanded (*i.e.* with circular holes) and compact (*i.e.* with elongated, almost closed elliptical holes) periodic configurations. Interestingly, in all these structures buckling is found to induce large negative values of incremental Poisson's ratio and in two of them also the formation of chiral patterns. Using a combination of finite element simulations and experiments at the centimeter scale we demonstrate a proof-of-concept of the proposed materials. Since the proposed mechanism for reconfigurable materials is induced by elastic instability, it is reversible, repeatable and scale-independent.

Mechanical instabilities are not always deleterious though they are conventionally regarded as failure modes. Because of the large deformation and dramatic shape changes that accompany them,[1,2] mechanical instabilities in elastic structures provide opportunities for designing responsive materials capable of reversibly switching between two different configurations with applications in sensors, microfluidics, bioengineering, robotics, acoustics and photonics.[3–8] In particular, instabilities in periodic porous structures comprising of square and triangular arrays of circular holes have been found to lead to the transformation of the pores in ordered arrays of high-aspect ratio (almost closed) ellipses[9–11] and have been demonstrated to be instrumental for the design of phononic switches,[7] color displays[12] and materials with unusual properties such as large negative Poisson's ratio.[13,14] However, to design the next generation of responsive and reconfigurable materials and devices that take advantage of the dramatic changes in geometry induced by instabilities, the effect of pore shape and lattice topology on the response of the system need to be fully understood. While it has been recently shown that the pore shape has a strong effect both on the onset of instability and on the postbuckling behavior,[13] there has been no systematic study on the effect of the hole arrangement. So far the selection of the architecture has been guided by intuition and buckling has been exploited as a folding mechanism only in square and triangular arrays of holes.[7,9,12–15]

Here, we first identify possible periodic distributions of monodisperse circular holes where buckling can be exploited to reversibly switch between expanded (*i.e.* with circular holes) and compact (*i.e.* with elongated, almost closed elliptical holes) periodic configurations. Then, we confirm the validity of our findings through a combination of experiments and numerical simulations. While two of these four configurations have been previously reported,[9,10,16] the other two are newly discovered. Remarkably, in these two new configurations elastic buckling not only can be exploited to design materials with negative Poisson's ratio (also known as auxetic material), but also acts as a reversible chiral symmetry-breaking mechanism, enabling the reversible switch between the initial nonchiral and the buckled chiral pattern. Furthermore, since the proposed folding mechanism exploits mechanical instabilities, our study opens avenues for the design of reconfigurable materials over a wide range of length scales.

We start by finding periodic monodisperse circular hole arrangements in plates where buckling can be exploited as a

[a]*School of Engineering and Applied Sciences, Harvard University, Cambridge, Massachusetts 02138, USA. E-mail: bertoldi@seas.harvard.edu; Fax: +1 617 495 9837; Tel: +1 617 496 3084*

[b]*Department of Civil, Structural and Environmental Engineering, University at Buffalo, Buffalo, NY 14260, USA*

[c]*Department of Physics, Harvard University, Cambridge, Massachusetts 02138, USA*

[d]*Wyss Institute for Biologically Inspired Engineering, Harvard University, Cambridge, Massachusetts 02138, USA*

[e]*Kavli Institute, Harvard University, Cambridge, Massachusetts 02138, USA*

† Electronic supplementary information (ESI) available. See DOI: 10.1039/c3sm51148k

‡ These authors contributed equally to this work.

mechanism to reversibly switch between undeformed/expanded and deformed/compact configurations. Therefore, we require that the instability does not only reduce the symmetry, but also leads to the transformation of the circular holes into elongated (almost closed) ellipses. Inspired by recent work on buckling of spherical structured shells, where hole arrangements were systematically explored through polyhedra,[6] here we investigate the hole arrangements by considering geometric constraints on the tilings (*i.e.*, tessellations) of the 2D Euclidean plane.

In order for all the monodisperse circular holes to close through buckling of the ligaments, the plates should meet the following requirements: (a) the center-to-center distances of adjacent holes are identical, so that all the ligaments are characterized by the same minimum width and undergo the first buckling mode in an approximately uniform manner; (b) there is an even number of ligaments around every hole, so that the deformation induced by buckling leads to their closure. Mathematically, these geometric constraints can be rephrased as: the skeleton of the porous structure should (a′) be a convex uniform tiling of the 2D Euclidean plane (which are vertex-transitive and have only regular faces) (b′) with an even number of faces meeting at each vertex. Focusing on convex uniform tilings (*i.e.* Platonic and Archimedean tilings) where all the vertices are the same, so that all the holes deform similarly, we find that there are only four tessellations which meet the above requirements: *square tiling*, *triangular tiling*, *trihexagonal tiling* and *rhombitrihexagonal tiling* (see Fig. 1A). Note that these tilings can be fully described by their vertex figures (*i.e.* a sequence of numbers representing the number of edges of the polygons going around the vertex): 4.4.4.4 for the square, 3.3.3.3.3.3 for the triangular, 3.6.3.6 for the trihexagonal and 3.4.6.4 for the rhombitrihexagonal tiling. The corresponding porous structures are then obtained by placing a circular hole at each vertex of the tiling (Fig. 1B and ESI†). To help us refer to these four periodic porous structures, hereafter we use the vertex figure of the corresponding tiling to denote them, as indicated in Fig. 1B. Fig. 1C shows the compact/folded configurations of the porous structures, which are obtained through finite element (FE) buckling analysis under uniaxial compression. They clearly show that all the ligaments in the structures undergo the first buckling mode uniformly. The instability is found not only to change the planar symmetry group of the structures (*i.e.* for 4.4.4.4 from *p*4*m* to *p*4*g*, for 3.3.3.3.3.3 from *p*6*m* to *pgg*, for 3.6.3.6 from *p*3*m*1 to *p*3, and 3.4.6.4 from *p*6*m* to *p*6), but also to lead to closure of the holes and compaction of the structures. It is worth noting that the same compact patterns can also be predicted using continuum elasticity theory and modeling each buckled elliptical hole as a dislocation dipole that interacts elastically with all the other dipoles in the system[17] (see ESI†).

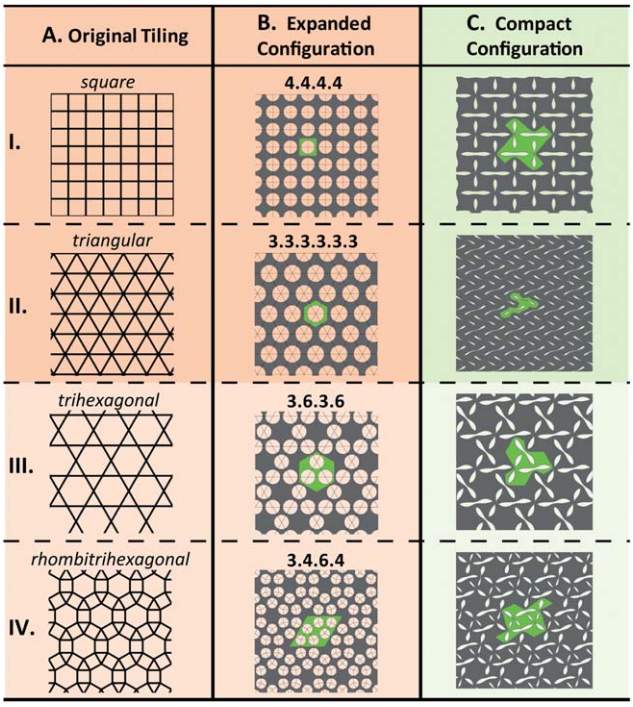

Fig. 1 Geometric compatibility for the arrangement of circular holes on the porous structures, restricted to four specific configurations (shown in each row). (A) Tilings. (B) Expanded undeformed porous structures. (C) Compact porous structures, which are buckled under uniaxial compression. The green-shaded regions in (B) and (C) denote the unit cell in the undeformed and deformed configurations, respectively.

Guided by our analysis, we built physical and numerical models of all four porous structures (see Fig. 2A). The structures are characterized by an initial void-volume-fraction $\psi_{4.4.4.4} = \psi_{3.6.3.3.6} = \psi_{3.4.6.4} = 0.49$ and $\psi_{3.3.3.3.3.3} = 0.48$ (ψ = total hole area/total area). Note that the slight variation in porosity between the four structures is related to limited accuracy during the fabrication process. The samples for the experiments were fabricated using silicone rubber with Young's modulus $E = 0.9$ MPa and a mold-casting process with molds prepared by 3D rapid prototyping. In all the structures, the holes are characterized by radius $r = 4$ mm and a large out-of-plane thickness is employed to avoid out-of-plane buckling. Uniaxial compression tests were performed on a standard quasi-static loading frame under displacement-control (see ESI† for details on the experimental setup). On the numerical side, simulations were performed using the non-linear Finite Element code ABAQUS/Standard. Plane strain conditions were assumed and the behavior of the silicone rubber used in the experiments was captured using the Yeoh hyperelastic model.[18] Uniaxial compression tests were simulated by imposing vertical displacements at the top face, while keeping all other degree of freedom of both top and bottom faces fixed (see ESI† for details on the FE simulations).

Representative pictures taken during the tests at different levels of nominal strain ε (calculated as change of height divided by the original height) are presented in Fig. 2, showing an excellent agreement between experiments and FE simulations. At small nominal strains, the holes are observed to deform uniformly (see Fig. 2B). However, when a critical value of applied nominal strain is reached, the thin ligaments between the holes start to buckle in a uniform manner. Eventually, at $\varepsilon = -0.15$ (Fig. 2C), a distinctive buckled pattern is observed in the central part of the samples, only marginally affected by the boundary conditions. Finally, the buckled pattern becomes further accentuated for larger values of applied

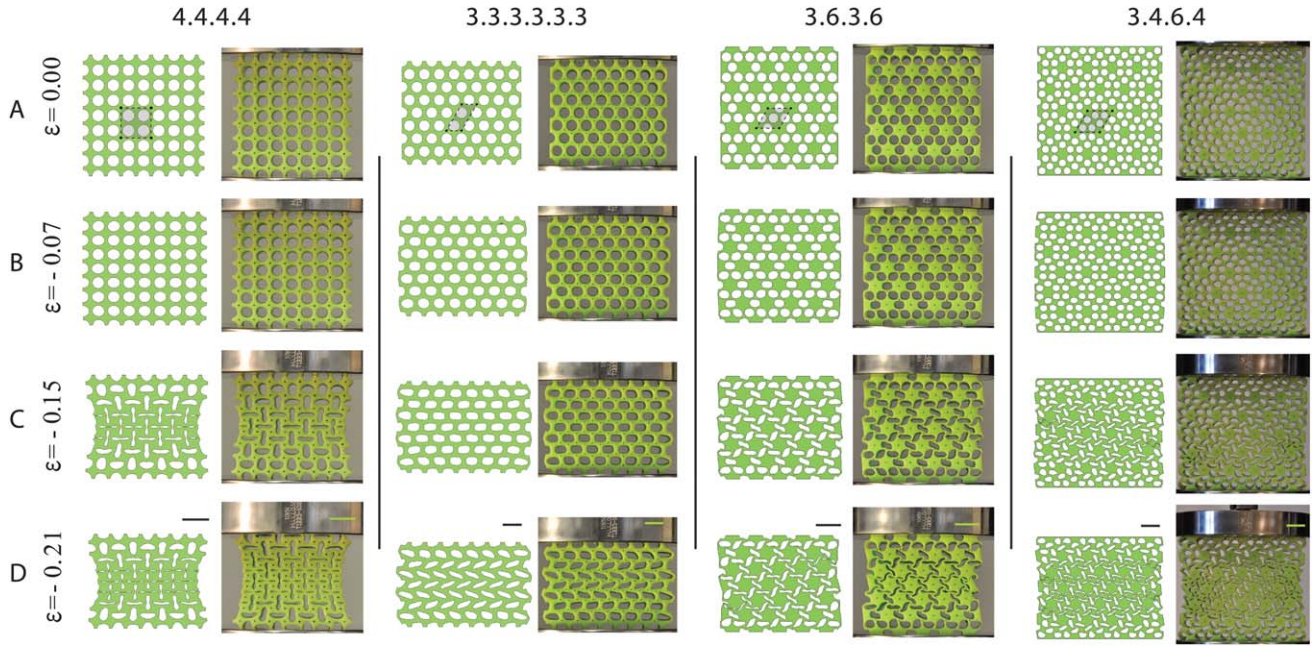

Fig. 2 Numerical (left) and experimental (right) images of all four structures (4.4.4.4, 3.3.3.3.3.3, 3.6.3.6 and 3.4.6.4) at different levels of deformation: (A) $\varepsilon = 0.00$, (B) $\varepsilon = -0.07$, (C) $\varepsilon = -0.15$ and (D) $\varepsilon = -0.21$. All configurations are characterized by an initial void-volume-fraction $\psi \approx 0.5$. Scale bars: 20 mm.

strain, leading to the formation of a periodic array of elongated, almost closed ellipses, as shown in Fig. 2D for $\varepsilon = -0.21$. Since the specimens are made of an elastomeric material, the process is fully reversible and repeatable. Upon release of the applied vertical displacement, the deformed structures recover their original configurations.

Interestingly, Figs. 2C–D clearly shows that the porous structures 3.6.3.6 and 3.4.6.4 buckle into a chiral pattern, while the initially expanded configurations are non-chiral. Therefore, in these two systems buckling acts as a reversible chiral symmetry breaking mechanism. Despite many studies on pattern formation induced by mechanical instabilities,[15] relatively little is known about the use of buckling as a reversible chiral symmetry breaking mechanism. Although several processes have been recently reported to form chiral patterns,[19–23] all of these work only at a specific length-scale, preventing their use for the formation of chiral structures over a wide range of length scales, as required by applications. Furthermore, most of these chiral symmetry breaking processes are irreversible[19–21] and only few systems have been demonstrated to be capable of reversibly switching between non-chiral and chiral configurations.[22,23] Remarkably, since the mechanism discovered here exploits a mechanical instability that is scale independent, our results raise opportunities for reversible chiral symmetry breaking over a wide range of length scales.

Both experiments and simulations reported in Fig. 2 clearly indicate that the onset of instability is strongly affected by the arrangement of the holes. A more quantitative comparison between the response of the structures investigated in this paper can be made by inspecting the evolution of stress during both experiments and simulations (see Fig. 3). Although all structures are characterized by roughly the same porosity, the hole arrangement is found to strongly affect both the effective modulus $\bar{E}$ (calculated as the initial slope of the stress–strain curves reported in Fig. 3) and the critical strain ε_{cr} (calculated as the strain at which the stress–strain curves reported in Fig. 3 plateau), demonstrating that through a careful choice of the

A

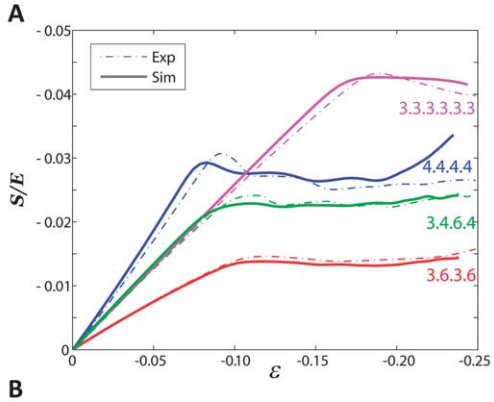

B

	4.4.4.4	3.3.3.3.3.3	3.6.3.6	3.4.6.4
$\overline{E}/E$ (Exp)	0.361	0.245	0.144	0.227
$\overline{E}/E$ (Sim)	0.373	0.254	0.145	0.234
ε_{cr} (Exp)	−0.090	−0.187	−0.112	−0.107
ε_{cr} (Sim)	−0.083	−0.169	−0.111	−0.097

Fig. 3 (A) Experimental and numerical stress–strain curves for the four structures. S denotes the nominal stress (calculated as force divided by the cross-sectional area in the undeformed configuration). Dashed lines correspond to experiments and solid lines to simulations. Note that for $\varepsilon < -0.20$ the porous structure 4.4.4.4. shows a stiffening behavior due to densification. A similar response is observed also for the other three structures, but for larger values of applied strain ε. (B) Table summarizing the mechanical properties of the four periodic structures measured from experiments and simulations.

architecture materials with the desired response can be designed.

A clear feature in Fig. 2 is that after instability the lateral boundaries of three samples (*i.e.* 4.4.4.4, 3.6.3.6 and 3.4.6.4) bend inwards, a clear sign of negative Poisson's ratio.[24,25] To quantify the lateral contraction (and thus the negative Poisson's ratio) of the porous structures, we investigate the evolution of the microstructure during both experiments and simulations. The physical samples were marked with black dots (see Fig. 2) and their position was recorded using a high-resolution digital camera and then analyzed by digital image processing (MATLAB). We focused on the central part of the samples where the response was clearly more uniform and marginally affected by the boundary conditions. For each structure we constructed several parallelograms connecting the markers in the central part of the sample (see Fig. 2A and 4A and ESI† for details) and monitored their evolution. For each parallelogram, local values of the engineering strain ε_{xx} and ε_{yy} were calculated from the positions of its vertices at each recorded frame t as

$$\varepsilon_{xx}(t) = \frac{(x_4(t) - x_3(t)) + (x_2(t) - x_1(t))}{2|\boldsymbol{L}^0_{34}|} - 1, \quad (1)$$

$$\varepsilon_{yy}(t) = \frac{(y_1(t) - y_3(t)) + (y_2(t) - y_4(t))}{2|\boldsymbol{L}^0_{13}|\cos\theta} - 1, \quad (2)$$

where (x_i, y_i) denote the coordinates of the i-th vertex of the parallelogram, $|\boldsymbol{L}^0_{34}|$ and $|\boldsymbol{L}^0_{13}|$ are the norm of the lattice vectors spanning the parallelogram in the undeformed configuration (see Fig. 4A) and $\theta = \arccos\frac{\boldsymbol{L}^0_{34}\cdot\boldsymbol{L}^0_{13}}{|\boldsymbol{L}^0_{34}||\boldsymbol{L}^0_{13}|}$. The local values of the engineering strain were then used to calculate local values of Poisson's ratio as

$$\nu(t) = -\frac{\varepsilon_{xx}(t)}{\varepsilon_{yy}(t)}, \quad (3)$$

and

$$\nu_{\mathrm{inc}}(t) = -\frac{\varepsilon_{xx}(t+\Delta t) - \varepsilon_{xx}(t)}{\varepsilon_{yy}(t+\Delta t) - \varepsilon_{yy}(t)}. \quad (4)$$

Note that ν characterizes the lateral contraction/expansion of the structure with respect to the initial/undeformed configuration. Differently, ν_{inc} quantifies the lateral contraction/expansion with respect to the deformed configuration induced by an increment in the applied strain $\Delta\varepsilon$ and allow us to describe the Poisson's ratio of a material that operates around a pre-deformed state. Finally, the ensemble averages $\bar{\varepsilon}_{\mathrm{xx}} = \langle\varepsilon_{\mathrm{xx}}\rangle$, $\bar{\varepsilon}_{\mathrm{yy}} = \langle\varepsilon_{\mathrm{yy}}\rangle$, $\bar{\nu} = \langle\nu\rangle$, and $\bar{\nu}_{\mathrm{inc}} = \langle\nu_{\mathrm{inc}}\rangle$ for the central parallelograms under consideration were computed.

On the numerical side, to verify that the values of $\bar{\nu}$ and $\bar{\nu}_{\mathrm{inc}}$ calculated from the experiments were not affected by the boundary conditions, we considered infinite periodic structures and investigated the response of representative volume elements (see insets in Fig. 4B) using periodic boundary conditions (see ESI† for details). The evolution of the macroscopic Poisson's ratio was then obtained from simulation using eqn (3) and (4), in this case with ε_{xx} and ε_{yy} denoting the macroscopic component of the strain.

The evolution of the Poisson's ratios $\bar{\nu}$ and $\bar{\nu}_{\mathrm{inc}}$ as function of the local engineering strain $\bar{\varepsilon}_{\mathrm{yy}}$ is presented in Fig. 4. As expected, all the structures are characterized by initially positive values of $\bar{\nu}$ and $\bar{\nu}_{\mathrm{inc}}$. However, as previously observed for a square array of circular holes,[13,14] the dramatic pattern transformation introduced by instability strongly affects the Poisson's ratio, leading to enhanced compaction. Beyond the instability, $\bar{\nu}$ is found to monotonically decrease as a function of $\bar{\varepsilon}_{\mathrm{yy}}$ in all the four structures and eventually becomes negative for three of them. While $\bar{\nu}$ gradually decrease after instability, $\bar{\nu}_{\mathrm{inc}}$ is characterized by two plateaus. Before instability setting on, all structure are characterized by a constant and positive value of $\bar{\nu}_{\mathrm{inc}} \approx 0.4$. At instability, a rapid transition to a negative value that then remains constant for increasing values of deformation is observed. More specifically, we find that after instability $\bar{\nu}_{\mathrm{inc4.4.4.4}} \approx -0.95$, $\bar{\nu}_{\mathrm{inc3.3.3.3.3.3}} \approx -0.39$, $\bar{\nu}_{\mathrm{inc3.6.3.6}} \approx -0.78$ and $\bar{\nu}_{\mathrm{inc3.4.6.4}} \approx -0.75$. Therefore, our results reveal that instabilities in the four periodic porous structures considered here can be exploited to design materials and devices whose response is characterized by large values of incremental negative Poisson's ratio $\bar{\nu}_{\mathrm{inc}}$. The material will exhibit such unusual behavior if pre-loaded beyond the instability point.

The results reported here clearly show that by carefully choosing the initial architecture, materials with unconventional response can be designed. In fact, our study demonstrates that buckling in four different periodic porous structures may be exploited to achieve large negative values of incremental

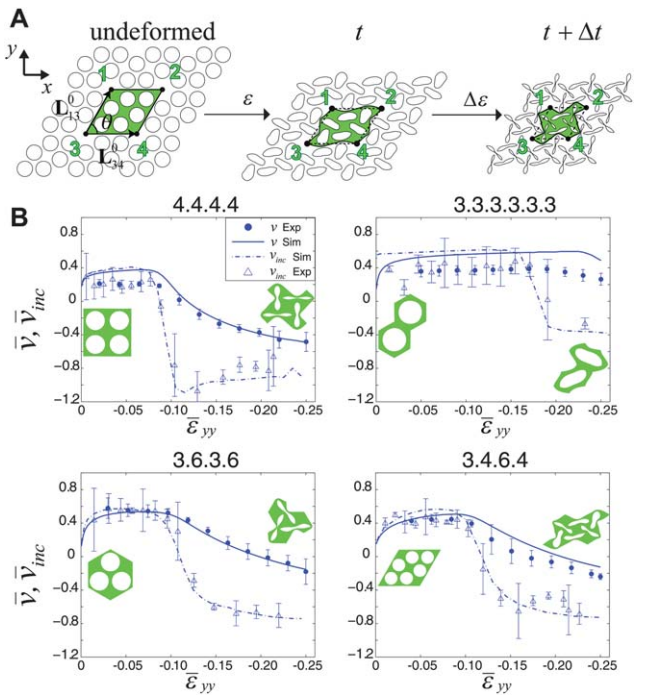

Fig. 4 (A) Schematic diagram of the central parallelograms used to compute $\bar{\nu}$ and $\bar{\nu}_{\mathrm{inc}}$. (B) Macroscopic Poisson's ratio $\bar{\nu}$ and $\bar{\nu}_{\mathrm{inc}}$ as a function of the local nominal strain $\bar{\varepsilon}_{\mathrm{yy}}$ for all the four periodic porous structures. Finite element simulations are performed on infinite periodic structures. Error-bars on experimental curves are standard deviation of the quantity calculated for multiple parallelograms in the central region (see ESI†).

Poisson's ratio and in two of them also to induce the formation of chiral patterns. Furthermore, while in this study we focused on the response of structures with $\psi \simeq 0.5$, the void-volume-fraction ψ can be also used to fine-tune the response of the structures, as revealed by previous studies.[13,14] To confirm the robustness of desired buckling phenomena, detailed FE simulations have been conducted to reveal that for structures with porosity in the range $\psi \in [0.4,0.6]$ buckling always lead to the compact configurations shown in Fig. 2C (see ESI†), demonstrating that the proposed folding mechanism can be effectively exploited to design a new class of reconfigurable materials.

In summary, we have identified four periodic distributions of mono-disperse circular holes in planar elastic structures where mechanical instability can be exploited to reversibly switch between expanded (*i.e.* with circular holes) and compact (*i.e.* with elongated, almost closed elliptical holes) configurations. Interestingly, in two of these structures (*i.e.* 3.6.3.6 and 3.4.6.4) the instability can be exploited to induce the formation of a chiral pattern. Furthermore, in all the structures the pattern transformation induced by instability is found to lead to large negative values of macroscopic Poisson's ratio. Also, due to the intrinsic characteristics of elastic buckling, our study opens avenues for the design of novel responsive and reconfigurable materials and devices over a wide range of length scales. In particular, recent developments in microscale fabrication open exciting opportunities for miniaturization of the proposed structures, with potential applications ranging from tunable mechanical metamaterials to switchable optics.

Finally we note that the design principles outlined in this paper, which combine concepts of topology (*i.e.* tilings) and mechanics (*i.e.* buckling), represent a powerful tool to design reconfigurable structures and can be further extended to curved surfaces and 3D structures.

This work has been supported by Harvard MRSEC through grant DMR-0820484 and by NSF through grants CMMI- 1149456 (CAREER) and by the Wyss Institute through the Seed Grant Program. K.B. acknowledges start-up funds from the Harvard School of Engineering and Applied Sciences and the support of the Kavli Institute and Wyss Institute at Harvard University. E.R.C. acknowledges NSF MSPRF grant DMS-1204686.

References

1 D. C. Hyun, G. D. Moon, E. C. Cho and U. Jeong, *Adv. Funct. Mater.*, 2009, **19**, 2155.
2 H. Yoon, A. Ghosh, J. Y. Han, S. H. Sung, W. B. Lee and K. Char, *Adv. Funct. Mater.*, 2012, **22**, 3723.
3 E. P. Chan, E. J. Smith, R. Hayward and A. J. Crosby, *Adv. Mater.*, 2008, **20**, 711–716.
4 T. S. Horozov, B. P. Binks, R. Aveyard and J. H. Clint, *Colloids Surf., A*, 2006, **282**, 377–386.
5 J. Kim, J. A. Hanna, M. Byun, C. D. Santangelo and R. C. Hayward, *Science*, 2012, **335**, 1201–1205.
6 J. Shim, C. Perdigou, E. R. Chen, K. Bertoldi and P. M. Reis, *Proc. Natl. Acad. Sci. U. S. A*, 2012, **109**, 5978–5983.
7 J. Jang, C. Koh, K. Bertoldi, M. Boyce and E. Thomas, *Nano Lett.*, 2009, **9**, 2113–2119.
8 S. Yang, K. Khare and P. C. Lin, *Adv. Funct. Mater.*, 2010, **20**, 2550.
9 T. Mullin, S. Deschanel, K. Bertoldi and M. C. Boyce, *Phys. Rev. Lett.*, 2007, **99**, 084301.
10 Y. Zhang, E. A. Matsumoto, A. Peter, P. C. Lin, R. D. Kamien and S. Yang, *Nano Lett.*, 2008, **8**, 1192–1196.
11 S. Singamaneni, K. Bertoldi, S. Chang, J. Jang, S. L. Young, E. L. Thomas, M. C. Boyce and V. V. Tsukruk, *Adv. Funct. Mater.*, 2009, **19**, 1426.
12 J. Li, J. Shim, J. Deng, J. Overvelde, X. Zhu, K. Bertoldi and S. Yang, *Soft Matter*, 2012, **8**, 10322.
13 J. Overvelde, S. Shan and K. Bertoldi, *Adv. Mater.*, 2012, **24**, 2337–2342.
14 K. Bertoldi, P. M. Reis, T. Willshaw and T. Mullin, *Adv. Mater.*, 2010, **22**, 361–366.
15 S. Singamaneni and V. V. Tsukruk, *Soft Matter*, 2010, **6**, 5681–5692.
16 K. Bertoldi, M. C. Boyce, S. Deschanel, S. M. Prange and T. Mullin, *J. Mech. Phys. Solids*, 2008, **56**, 2642–2668.
17 E. A. Matsumoto and R. D. Kamien, *Phys. Rev. E: Stat., Nonlinear, Soft Matter Phys.*, 2009, **80**, 021604.
18 O. H. Yeoh, *Rubber Chem. Technol.*, 1993, **66**, 754–771.
19 E. Edlund, O. Lindgren and M. N. Jacobi, *Phys. Rev. Lett.*, 2012, **108**, 165502.
20 B. Pokroy, S. H. Kang, L. Mahadevan and J. Aizenberg, *Science*, 2009, **323**, 237–240.
21 S. Ferjani, Y. Choi, J. Pendery, R. Petschek and C. Rosenblatt, *Phys. Rev. Lett.*, 2010, **104**, 257801.
22 D. Grohol, K. Matan, J. H. Cho, S. H. Lee, J. W. Lynn, D. G. Nocera and Y. S. Lee, *Nature Mater.*, 2005, **4**, 323–328.
23 D. R. Link, G. Natale, R. Shao, J. E. Maclennan, N. A. Clark, E. Korblova and D. M. Walba, *Science*, 1997, **278**, 1924–1927.
24 R. Lakes, *Science*, 1987, **235**, 1038–1040.
25 K. E. Evans and A. Alderson, *Adv. Mater.*, 2000, **12**, 617–628.

Electronic Supplementary Material (ESI) for Soft Matter

Supporting Information for
Harnessing instabilities for design of soft reconfigurable auxetic/chiral materials

Jongmin Shim,[1,2] Sicong Shan,[3,2] Andrej Košmrlj,[4] Sung H. Kang,[3]
Elizabeth R. Chen,[3] James C. Weaver,[5] and Katia Bertoldi[3,6]

[1]*Department of Civil, Structural and Environmental Engineering, University at Buffalo, NY, 14260, USA*
[2]*J.S. and S.S. contributed equally to this work*
[3]*School of Engineering and Applied Sciences, Harvard University, Cambridge, Massachusetts 02138, USA*
[4]*Department of Physics, Harvard University, Cambridge, Massachusetts 02138, USA*
[5]*Wyss Institute for Biologically Inspired Engineering, Harvard University, Cambridge, Massachusetts 02138, USA*
[6]*Kavli Institute, Harvard University, Cambridge, Massachusetts 02138, USA*

ANALYSIS - DESIGN PRINCIPLES

From tilings of the 2D Euclidean plane to porous structures

To identify possible periodic monodisperse circular hole arrangements in elastic plates where buckling can be exploited as a mechanism to reversibly switch between undeformed/expanded and deformed/compact configurations, we investigate the hole arrangements by considering geometric constraints on the tilings (i.e., tessellations) of the 2D Euclidean plane.

In order for all the monodisperse circular holes to close through buckling of the ligaments, the plates should meet the following requirements: (a) the center-to-center distances of adjacent holes are identical, so that all the ligaments are characterized by the same minimum width and undergo the first buckling mode in an approximately uniform manner; (b) there is an even number of ligaments around every hole, so that the deformation induced by buckling leads to their closure. Mathematically, these geometric constraints can be rephrased as: the skeleton of the porous structure should (a') be a convex uniform tiling of the 2D Euclidean plane (which are vertex-transitive and have only regular faces) (b') with an even number of faces meeting at each vertex. Focusing on 1-uniform tilings (i.e. Archimedean tilings) where all the vertices are the same, so that all the holes deform similarly, we find that there are only four tessellations which meet the above requirements: *square tiling*, *triangular tiling*, *trihexagonal tiling* and *rhombitrihexagonal tiling* (see Fig. S1-A). The corresponding porous structures are then obtained by placing a circular hole at each vertex of the four tilings (see Fig. S1-B). Finally, we note that each periodic porous structure has an underlying kinematic model which comprises of a network of rigid polygons and hinges (see Fig. S1-C). These kinematic models can be obtained by transforming the circular holes either to (*i*) squares, if they are surrounded by four thin ligaments (as in the cases of 4.4.4.4, 3.6.3.6, 3.4.6.4); or (*ii*) hexagons, if they are surrounded by six thin ligaments (as in the cases of 3.3.3.3.3.3).

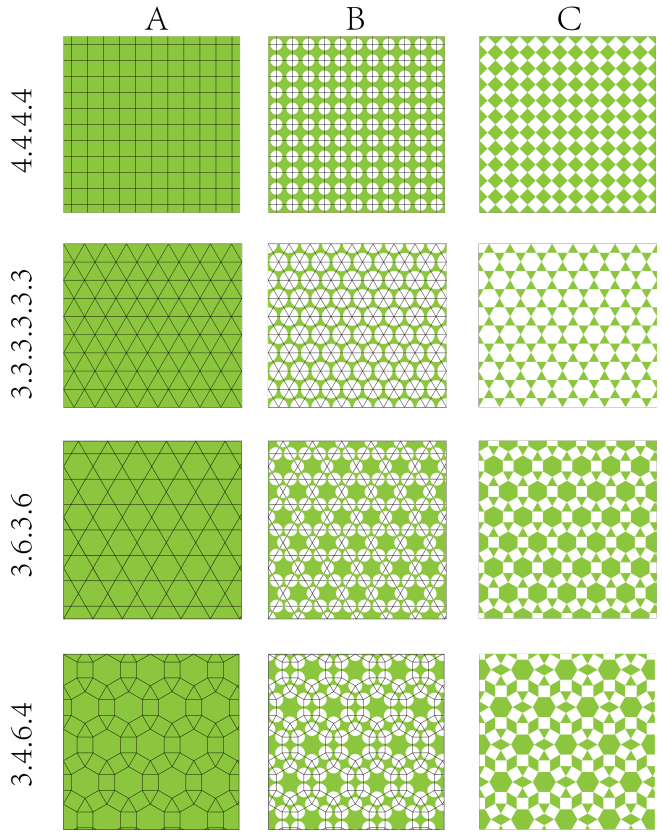

Figure S1: From tilings to porous structures. (A) We start with a solid sheet of material and draw a tiling pattern on the sheet. (B) The corresponding porous structure is then obtained by placing a circular hole at each vertex of the tiling. (C) The corresponding kinematic model can be obtained by transforming the circular holes either to squares or hexagons.

The kinematic models can then be used to study the deformation mechanism of the corresponding porous structures. Fig. S2 shows the folding mechanism of the four kinematic models investigated in this study.

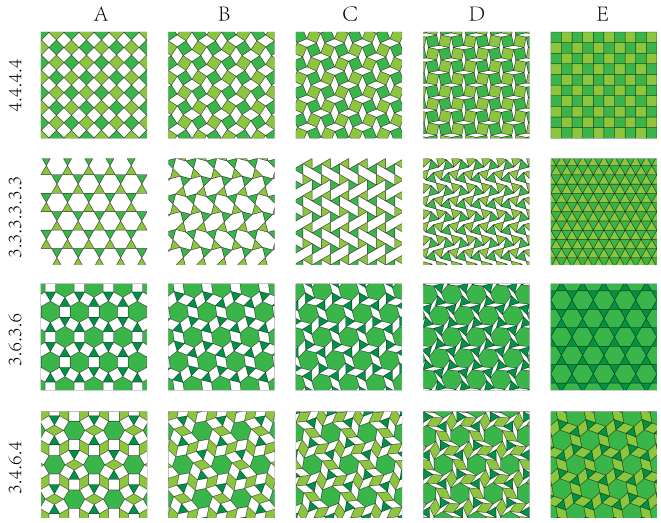

Figure S2: Folding mechanism of the kinematic models. (A) completely unfolded configuration; (B),(C) and (D) intermediate configurations; (E) completely compact/folded configuration. The polygons are colored differently only for visualization purposes.

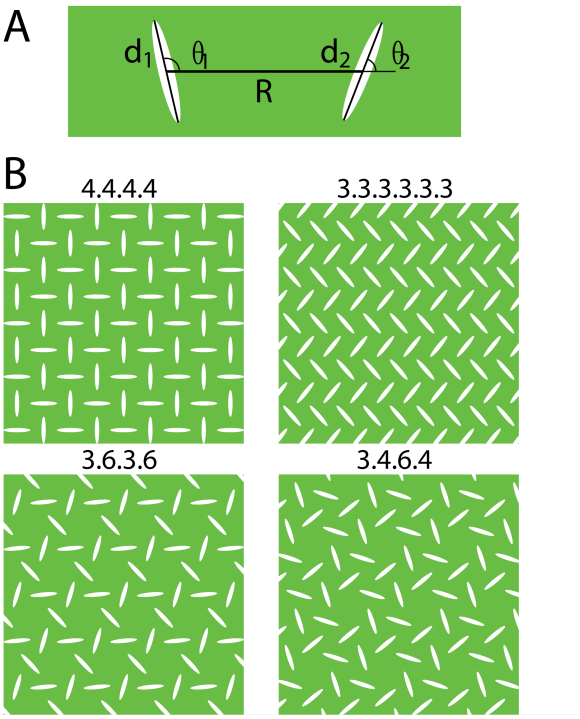

Figure S3: (A) Diagram of the interaction between two elastic dipoles (d_1 and d_2) separated by R. (B) Patterns that correspond to the minimum free energy of interactions between elastic dipoles for the four structures considered in this study.

DISLOCATION DIPOLE MODEL

It has been recently shown that the patterns induced by buckling in periodic porous structures can be investigated by making use of continuum elasticity theory and approximating the deformed holes as elastic dipoles [1]. The stress fields due to elastic dipoles are long ranged and dipoles interact with each other with interaction energy [1]

$$U_{\text{int}} = -\frac{E}{\pi}\frac{b^2 d_1 d_2}{R^2}\left[\cos\left(\theta_1+\theta_2\right)\sin\theta_1\sin\theta_2+\frac{1}{4}\right], \tag{S1}$$

where E is the 2-dimensional Young's modulus of bulk elastic medium, R is distance between two dipoles, d_1 and d_2 are magnitudes of dipole vectors, and θ_1 and θ_2 are dipole orientations (Fig. S3A). We note that individual elastic dipoles also feel the effect of the external uniaxial compression [1], but this contribution is neglected in this study. Assuming periodic boundary conditions and independent orientations of dipoles inside the primitive cell (Fig. S6), we minimized the interaction energy of elastic dipoles (S1). For each dipole, we included interactions with $\sim$ 100 nearest dipole neighbors. The patterns that correspond to the minimized interaction energy of elastic dipoles in the four arrangements investigated in this study are shown in Fig. S3. The patterns closely resemble the patterns obtained with FE analysis (see Fig. 1-C).

EXPERIMENTS

Material

Silicone rubber (Vinylpolysiloxane: Elite Double 32, Zhermack) was used to cast the experimental specimens. The material properties were measured through tensile testing, up to a nominal strain $\epsilon = 0.82$. No hysteresis and rate dependence was found during loading and unloading. The stress-strain behavior was found to be accurately captured by a Yeoh hyperelastic model [2], whose strain energy density is

$$W_{\text{Yeoh}} = \sum_{i=1}^{3}\left[C_{i0}\left(\bar{I}_1-3\right)^i+\left(J-1\right)^{2i}/D_i\right] \tag{S2}$$

where $\bar{I}_1 = \text{tr}\left[\text{dev}\left(\mathbf{F}^T\mathbf{F}\right)\right]$, $J = \det\left[\mathbf{F}\right]$, and $\mathbf{F}$ is the deformation gradient. Note that two of the parameters entering in Yeoh model are related to the conventional shear modulus (G_0) and bulk modulus (K_0) at zero strain as $C_{10} = G_0/2$ and $D_1 = 2/K_0$. To capture the behavior of the silicone rubber used in the experiments we used $C_{10} = 154\ kPa$, $C_{20} = 0\ kPa$, $C_{30} = 3.5\ kPa$, and $D_1 = D_2 = D_3 = 38.2\ GPa^{-1}$.

Specimens fabrication

The molds to cast the specimens were fabricated using a 3-D printer (Connex 500, Objet Ltd.) having a resolution of 600 *dpi* and a claimed printing accuracy of 30 μm. A very thin layer of mold release oil (Ease Release 200, Smooth-on Inc.) was sprayed onto the mold prior to molding. Then, the silicone rubber was cast into the mold. The casted mixture was first allowed to set in a vacuum for 10 minutes and then was placed at room temperature until curing was completed. The overall sizes of the four specimens are $W(\text{width}) \times H(\text{height}) \times T(\text{thickness}) = 80.0 \times 80.0 \times 35.0mm, 86.6 \times 75.0 \times 35.0mm, 93.3 \times 97.0\ mm \times 35.0\ mm$ and $132.0 \times 137.1\ mm \times 55.0\ mm$ for 4.4.4.4, 3.3.3.3.3.3, 3.6.3.6, 3.4.6.4, respectively. Note that large out-of-plane thicknesses were employed for all the specimens in order to avoid out-of-plane buckling modes during the uniaxial compression tests. The four samples were designed to have a void-volume-fraction $\psi = 0.50$ and holes with radius $r = 4.0\ mm$. This resulted in a center-to-center distance between adjacent holes of $a = 10.8\ mm$ for the 3.3.3.3.3.3 pattern, $a = 9.3\ mm$ for the 3.6.3.6 pattern, and $a = 9.7\ mm$ for the 3.4.6.4 pattern. Note that the fabricated samples were found to have a slightly lower void-volume-fraction (i.e. $\psi_{4.4.4.4} = 0.49$, $\psi_{3.3.3.3.3.3} = 0.48$, $\psi_{3.6.3.6} = 0.49$, $\psi_{3.4.6.4} = 0.49$), due to the limited accuracy of the 3D printer. This deviation has been accounted for in the simulations.

Testing

Uniaxial compressive experiments were performed on a standard quasi-static loading frame (Instron 5566) with a 10 kN load cell (Instron 2710-106) in a displacement-controlled manner. The specimens were compressed within flat compression fixtures. Note that the specimen was not clamped to the fixtures, but friction between the specimen and fixture surface was enough to hold the position of the specimens' top and bottom faces because no lubricant was used on the horizontal surfaces. The compression tests were performed at the cross-head velocity of 20 mm/min until the holes were almost closed. During the test, a Nikon D90 SLR camera facing the specimen was used to take pictures at every nominal strain increment of $\Delta\epsilon = 0.006$. The specimens were marked with black dots, so that we were able to quantify the changes in the geometry of the structures induced by deformation with a post-processing code in MATLAB.

Calculation of $\bar{\epsilon}_{xx}$, $\bar{\epsilon}_{yy}$, $\bar{\nu}$ and , $\bar{\nu}_{inc}$ from experiments

To quantify the lateral contraction (and thus the negative Poisson's ratio) of the porous structures in experiments, we investigated the evolution of the microstructure. The physical samples were marked with black dots as shown in Fig. 2 in the main text and their position was recorded using a high-resolution digital camera and then analyzed by digital image processing (MATLAB). All the black markers were identified in the initial frame (Fig. S4-A), and followed through the loading process. We only focused on the central part of the samples where the response was clearly more uniform and marginally affected by the boundary conditions. We first constructed several parallelograms connecting the markers in the central part of the sample (Fig. S4-B) and monitored their evolution as a function of the applied deformation. All the markers and their corresponding parallelograms which were used in the calculations, are highlighted in green in Fig. S4-C. For each parallelogram, local values of the engineering strain ϵ_{xx} and ϵ_{yy} were calculated from the positions of its vertices at each recorded frame t as

$$\epsilon_{xx}(t) = \frac{(x_4(t) - x_3(t)) + (x_2(t) - x_1(t))}{2 \mid \mathbf{L}^0_{34} \mid} - 1, \qquad \text{(S3)}$$

$$\epsilon_{yy}(t) = \frac{(y_1(t) - y_3(t)) + (y_2(t) - y_4(t))}{2 \mid \mathbf{L}^0_{13} \mid \cos\theta} - 1, \qquad \text{(S4)}$$

where $(x_i,\ y_i)$ denote the coordinates of the i-th vertex of the parallelogram, $\mid \mathbf{L}^0_{34} \mid$ and $\mid \mathbf{L}^0_{13} \mid$ are the norm of the lattice vectors spanning the parallelogram in the undeformed configuration (see Fig. 4-A in the main text) and $\theta = \arccos \frac{\mathbf{L}^0_{34} \cdot \mathbf{L}^0_{13}}{|\mathbf{L}^0_{34}||\mathbf{L}^0_{13}|}$. The local values of the engineering strain were then used to calculate local values of the Poisson's ratio as

$$\nu(t) = -\frac{\epsilon_{xx}(t)}{\epsilon_{yy}(t)}, \qquad \text{(S5)}$$

and

$$\nu_{inc}(t) = -\frac{\epsilon_{xx}(t + \Delta t) - \epsilon_{xx}(t)}{\epsilon_{yy}(t + \Delta t) - \epsilon_{yy}(t)}. \qquad \text{(S6)}$$

Note that ν characterizes the lateral contraction/expansion of the structure with respect to the initial/undeformed configuration. Differently, ν_{inc} quantifies the lateral contraction/expansion with respect to the deformed configuration induced by an increment in the applied strain $\Delta\epsilon$ and allow us to describe the Poisson's ratio of a material that operates around a pre-deformed state. Finally, the ensemble averages $\bar{\epsilon}_{xx} =< \epsilon_{xx} >$, $\bar{\epsilon}_{yy} =< \epsilon_{yy} >$, $\bar{\nu} =< \nu >$ and , $\bar{\nu}_{inc} =< \nu_{inc} >$ for the central parallelograms under consideration were computed.

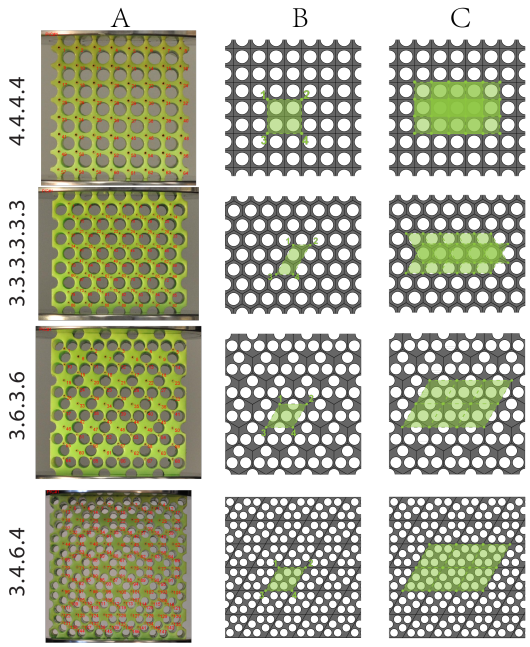

Figure S4: Illustration of calculation of $\overline{\epsilon}_{xx}$, $\overline{\epsilon}_{yy}$, $\overline{\nu}$ and $\overline{\nu}_{inc}$ from experiments. (A) The samples were marked with black dots. These markers were identified with a tracking number in the initial frame and followed through the loading process. (B) Parallelograms connecting four markers in the central part of the sample were constructed and their evolution was monitored as a function of the applied deformation. (C)All the parallelograms used in the calculations are highlighted in green.

FINITE-ELEMENT SIMULATIONS

Load-displacement analysis

The commercial finite element (FE) code ABAQUS/Standard was used for simulating the post-buckling response of the finite-size porous structures. Assuming plane strain conditions, 2D FE models were constructed using ABAQUS element type *CPE6MH* with a mesh sweeping seed size of 0.5 mm.

After determining the pattern transformation (the lowest eigenmode) from a buckling analysis, an imperfection in the form of the most critical eigenmode was introduced into the mesh, scaled so that its magnitude was two orders of magnitude smaller than the hole size.

As the experiments were performed under displacement-controlled conditions, load-displacement analysis were then performed imposing vertical displacements at the top surface of the FE model, while fixing the horizontal degrees of freedom. All the degrees of freedom of the bottom surface were fixed.

Instability Analysis for Infinitely Periodic Solids

Our results demonstrate that buckling in elastic plates with carefully designed arrangement of holes may be exploited to induce either the formation of chiral patterns and/or negative Poisson's ratio. However, so far we only focused on the response of structures with $\psi \simeq 0.5$, and did not explore the effect of the void-volume-fraction ψ, which can be used to control the critical strain at buckling. Since our results clearly show that the FE simulations were able to accurately reproduce the experimental results, we investigated numerically the effect of ψ on the instability of the structured plates. For the sake of computation efficiency, we focused on infinite periodic structures, and performed all the analysis on a single unit cell using appropriate boundary conditions [3, 4]. It is well known that along the loading path periodic structures can suddenly change their periodicity due to either microscopic instability (*i.e.*, instability with wavelengths that are of the order of the size of the microstructure) or macroscopic instability (*i.e*, instability with much larger wavelengths than the size of the microstructure) [3, 4]. In the following we provide a detailed description of the numerical analysis performed to detect both microscopic and macroscopic instabilities.

Infinite periodic structures In this section, we consider infinite planar periodic solids under plane strain conditions (Fig. S5-A). The periodic solid is characterized by a unit cell spanned by the lattice vectors $\mathbf{A}_1$ and $\mathbf{A}_2$ in the undeformed configuration (Fig. S5-B) and any spatial function $V(\mathbf{X})$ must satisfy the periodic condition

$$V(\mathbf{X}+\mathbf{R}) = V(\mathbf{X}) \tag{S7}$$

where with $\mathbf{R} = p_1\mathbf{A}_1 + p_2\mathbf{A}_2$, p_1 and p_2 being integers. For later use, we also introduce the reciprocal lattice vectors (Fig. S5-C)

$$\mathbf{B}_1 = 2\pi \frac{\mathbf{A}_2 \times \mathbf{A}_3}{||\mathbf{A}_1 \times \mathbf{A}_2||}, \quad \mathbf{B}_2 = 2\pi \frac{\mathbf{A}_3 \times \mathbf{A}_1}{||\mathbf{A}_1 \times \mathbf{A}_2||} \tag{S8}$$

where $\mathbf{A}_3 = (\mathbf{A}_1 \times \mathbf{A}_2)/||\mathbf{A}_1 \times \mathbf{A}_2||$, so that $\mathbf{A}_i \cdot \mathbf{B}_j = 2\pi\delta_{ij}$, δ_{ij} being the Kronecker delta. Thus, the reciprocal lattice vector $\mathbf{G}$ can be expressed by $\mathbf{G} = q_1\mathbf{B}_1 + q_2\mathbf{B}_2$, q_1 and q_2 being integers. Figure S5-C illustrates the reciprocal unit spanned by the primitive reciprocal lattice vectors $\mathbf{B}_1$ and $\mathbf{B}_2$.

Incremental formulation The deformation of the unit cell is described by the deformation gradient

$$\mathbf{F} = \frac{\partial \mathbf{x}}{\partial \mathbf{x}_0}, \tag{S9}$$

mapping a point in the material from the reference position $\mathbf{x}_0$ to its current location $\mathbf{x}$. The material is assumed

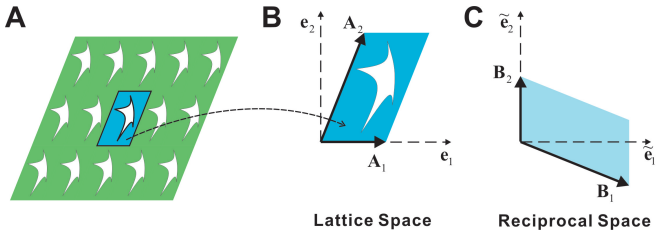

Figure S5: (A) Schematic of infinite periodic structure in two dimensional space. (B) Primitive unit spanned by the primitive lattice vectors $\mathbf{A}_1$ and $\mathbf{A}_2$. Basis vectors are denoted by $\mathbf{e}_1$ and $\mathbf{e}_2$. (C) The corresponding reciprocal unit spanned by the primitive reciprocal lattice vectors $\mathbf{B}_1$ and $\mathbf{B}_2$. Basis vectors $\widetilde{\mathbf{e}}_i$ are defined by $\widetilde{\mathbf{e}}_i = \frac{2\pi}{||\mathbf{A}_1 \times \mathbf{A}_2||}\ \mathbf{e}_i$ for $i = 1, 2$.

to be non-linear elastic, characterized by a stored-energy function $W = W(\mathbf{F})$, which is defined in the reference configuration. The first Piola-Kirchhoff stress $\mathbf{S}$ is thus related to the deformation gradient $\mathbf{F}$ by

$$\mathbf{S} = \frac{\partial W}{\partial \mathbf{F}}. \tag{S10}$$

In the absence of body forces, the equation of motions in the reference configuration can be written as

$$\mathrm{Div}\,\mathbf{S} = \rho_0 \frac{D^2\mathbf{x}}{Dt^2}, \tag{S11}$$

where Div represents the divergence operator in the undeformed/reference configuration, D/Dt is the material time derivative and ρ_0 denotes the reference mass density.

To investigate the stability of the periodic solid, incremental deformations superimposed upon a given state of finite deformation are considered. Denoting with $\dot{\mathbf{S}}$ the increment of the first Piola-Kirchhoff stress, the incremental forms of the governing equations is given by

$$\mathrm{Div}\,\dot{\mathbf{S}} = \rho_0 \frac{D^2\dot{\mathbf{x}}}{Dt^2}, \tag{S12}$$

where $\dot{\mathbf{x}}$ denotes the incremental displacements. Furthermore, linearization of the constitutive equation (S10) yields

$$\dot{\mathbf{S}} = \mathbb{L} : \dot{\mathbf{F}}, \quad \text{with } \mathbb{L}_{ijkl} = \frac{\partial^2 W}{\partial F_{ij} \partial F_{kl}}, \tag{S13}$$

where $\dot{\mathbf{F}}$ denotes the incremental deformation gradient, and $\mathbb{L}$ denotes incremental modulus (*i.e.* elasticity tensor).

To detect microscopic instabilities, we investigate the propagation of small-amplitude elastic waves defined by

$$\dot{\mathbf{x}}(\mathbf{X}, t) = \dot{\tilde{\mathbf{x}}}(\mathbf{X}) \exp(-i\omega t)\ , \tag{S14}$$

where ω is the angular frequency of the propagating wave, and $\dot{\tilde{\mathbf{x}}}$ denotes the magnitude of the incremental displacement. It follows from (S13) that

$$\dot{\mathbf{S}}(\mathbf{X}, t) = \dot{\tilde{\mathbf{S}}}(\mathbf{X}) \exp(-i\omega t)\ , \tag{S15}$$

so that equations (S12) become

$$\mathrm{Div}\dot{\tilde{\mathbf{S}}} = \rho_0\, \omega^2 \dot{\tilde{\mathbf{x}}}\ , \tag{S16}$$

which represent the frequency-domain wave equations.

Microscopic instabilities Although microscopic (local) buckling modes may alter the initial periodicity of the solid, they can be still detected by studying the response of a single unit cell and investigating the propagation of small-amplitude waves with arbitrary wave vector $\hat{\mathbf{K}}$ superimposed on the current state of deformation [5, 6]. While a real angular frequency ω corresponds to a propagating wave, a complex ω identifies a perturbation exponentially growing with time. Therefore, the transition between a stable and an unstable configuration is detected when the frequency vanishes (i.e. $\omega = 0$) and the new periodicity of the solid introduced by instability can be easily obtained by the corresponding wave vector.

To detect the onset of microscopic instabilities, we first deform the primitive unit cell to a certain extent and then investigate the propagation of elastic waves with different wave vector

$$\hat{\mathbf{K}} = \hat{K}_1 \mathbf{B}_1 + \hat{K}_2 \mathbf{B}_2, \tag{S17}$$

$\hat{K}_1$ and $\hat{K}_2$ being two real numbers. For each wave vector $\hat{\mathbf{K}}$, the angular frequency ω is determined by solving the frequency domain equation (S16). In this analysis quasi-periodic boundary conditions are applied, so that

$$\dot{\tilde{\mathbf{x}}}(\mathbf{X} + \hat{\mathbf{R}}) = \dot{\tilde{\mathbf{x}}}(\mathbf{X}) \exp(i\hat{\mathbf{K}} \cdot \hat{\mathbf{R}}), \tag{S18}$$

$\hat{\mathbf{R}}$ denoting the distance in the current configuration between each pair of nodes periodically located on the boundary. Since most commercial finite-element packages do not support the complex-valued displacements introduced by (S18), following Aberg and Gudmundson [7] we split any complex-valued spatial function $\phi(\mathbf{X})$ into a real and an imaginary part,

$$\phi(\mathbf{X}) = \phi(\mathbf{X})^{re} + i\phi(\mathbf{X})^{im}. \tag{S19}$$

The problem is then solved using two identical finite-element meshes for the unit cell, one for the real part and the other for the imaginary part, coupled by

$$\dot{\tilde{\mathbf{x}}}^{re}(\mathbf{X} + \hat{\mathbf{R}}) = \dot{\tilde{\mathbf{x}}}^{re}(\mathbf{X}) \cos(\hat{\mathbf{K}} \cdot \hat{\mathbf{R}}) - \dot{\tilde{\mathbf{x}}}^{im}(\mathbf{X}) \sin(\hat{\mathbf{K}} \cdot \hat{\mathbf{R}}), \tag{S20}$$

$$\dot{\tilde{\mathbf{x}}}^{im}(\mathbf{X} + \hat{\mathbf{R}}) = \dot{\tilde{\mathbf{x}}}^{re}(\mathbf{X}) \sin(\hat{\mathbf{K}} \cdot \hat{\mathbf{R}}) + \dot{\tilde{\mathbf{x}}}^{im}(\mathbf{X}) \cos(\hat{\mathbf{K}} \cdot \hat{\mathbf{R}}). \tag{S21}$$

A microscopic instability is detected at the first point along the loading path for which a wave vector $\hat{\mathbf{K}}_{cr} = \hat{K}_{1,cr}\mathbf{B}_1 + \hat{K}_{2,cr}\mathbf{B}_2$ exist such that the corresponding angular frequency ω is zero. The instability will result in an enlarged unit cell with $n_1 \times n_2$ primitive unit cells, where

$$n_1 = \frac{1}{\hat{K}_{1,cr}}, \quad \text{and} \quad n_2 = \frac{1}{\hat{K}_{2,cr}}. \tag{S22}$$

Macroscopic instabilities Following Geymonat et al. [5], we investigate macroscopic instabilities by detecting loss of strong ellipticity of the overall response of the periodic structure. Specifically, macroscopic instabilities may develop whenever the condition

$$(\mathbf{m}\otimes\mathbf{M}) : \left[\mathbb{L}^H : (\mathbf{m}\otimes\mathbf{M})\right] > 0 \ , \quad \text{for all} \quad \mathbf{m}\otimes\mathbf{M} \neq \mathbf{0} \tag{S23}$$

is first violated along the loading path, $\mathbb{L}^H$ denoting the homogenized incremental modulus.

In this study, 2D FE simulations on the primitive cell (see Fig. S6) are performed to detect macroscopic instabilities applying periodic boundary conditions (S7). Operationally, after determining the principal solution, the components of $\mathbb{L}^H$ are identified by subjecting the unit cells to four independent linear perturbations of the macroscopic deformation gradient [6]. Then loss of ellipticity is examined by checking condition (S23) at every $\pi/360$ radian increment.

Results Here, FE simulations are performed to compute both microscopic and macroscopic instabilities under uniaxial compression for structures characterized by a wide range of void-volume-fractions, $\psi \in (0.4, 0.6)$. Note that higher levels of porosity would lead to structures characterized by very thin ligaments, making them fragile. On the other hand, for smaller values of porosity the response of the structures would be highly affected by the material nonlinearity.

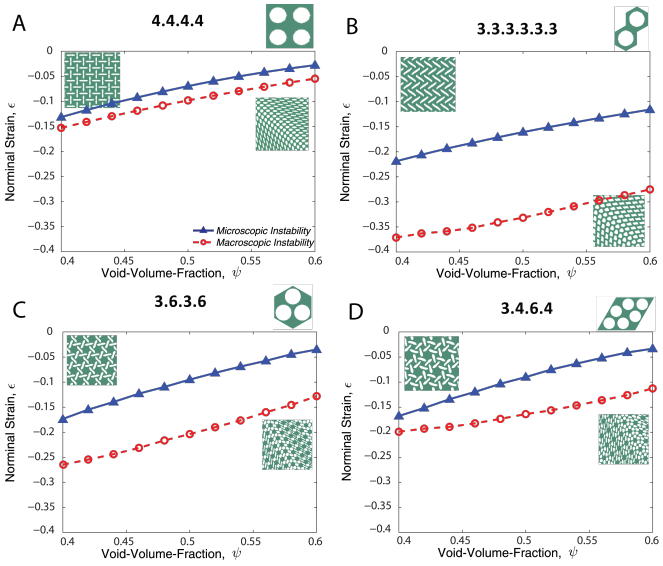

Figure S6: Nominal strain ϵ at the onset of microscopic and macroscopic instabilities as a function of the void-volume-fraction ψ. The results confirm that microscopic buckling is always critical with for the considered range of ψ.

The results of the instability analyses are summarized in Fig. S6, where the critical strain for both macroscopic and microscopic instability is reported as a function of ψ. As expected, the critical nominal strains at instability decrease for increasing values of ψ due to the reduction of the structural stiffness regardless of the types of instability. Interestingly, within the considered range of void-volume-fraction for all configurations the critical nominal strains for microscopic instability is found to be always smaller than that for macroscopic instability. Thus, these results indicate that for all configurations the folded patterns induced by microscopic buckling will emerge for a wide range of void-volume-fraction.

[1] E. A. Matsumoto and R. D. Kamien, Phys. Rev. E **80**, 021604 (2009).
[2] O. H. Yeoh, Rubber Chem. Technol. **66**, 754 (1993).
[3] N. Triantafyllidis and B. N. Maker, J. Appl. Mech. - T. ASME **52**, 794 (1985).
[4] K. Bertoldi and M. C. Boyce, Phys. Rev. B **78**, 184107 (2008).
[5] G. Geymonat, S. Muller, and N. Triantafyllidis, Arch. Ration. Mech. Anal. **122**, 231 (1993).
[6] K. Bertoldi, M. C. Boyce, S. Deschanel, S. M. Prange, and T. Mullin., J. Mech. Phys. Solids **56**, 2642 (2008).
[7] M. Åberg and P. Gudmundson, J. Acoust. Soc. Am. **102**, 2007 (1997).